NANO LETTERS

General Syntheses of High-Performance Thermoelectric Nanostructured Solids without Post-Synthetic Ligand Stripping

Yue Lou,[⊥] Xiaokun Li,[⊥] Zhan Shi, Hao Zhou, Tianli Feng, and Biao Xu[*]

Cite This: *Nano Lett.* 2023, 23, 5317−5325 **Read Online**

ACCESS | Metrics & More | Article Recommendations | Supporting Information

ABSTRACT: Ligand-assisted wet chemical synthesis is a versatile methodology to produce controllable nanocrystals (NCs). The post-treatment of ligands is significant for the performance of functional devices. Herein, a method that retains ligands of colloidal-synthesized nanomaterials to produce thermoelectric nanomaterials is proposed, which differs from the conventional methods that strip ligands using multistep cumbersome processes. The ligand-retention method can control the size and dispersity of nanocrystals during the consolidation of the NCs into dense pellets, in which retained ligands are transformed into organic carbon within the inorganic matrices, establishing clear organic−inorganic interfaces. Characterizations of the nonstripped and stripped samples confirm that this strategy can affect electric transport slightly but reduce the thermal conductivity largely. As a result, the materials (e.g., SnSe, $Cu_{2-x}S$, $AgBiSe_2$, and $Cu_2ZnSnSe_4$) with ligands retained achieve higher peak zT and better mechanical properties. This method can be applied to other colloidal thermoelectric NCs and functional materials.

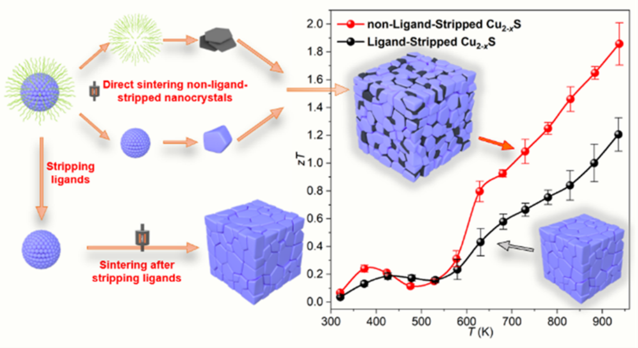

KEYWORDS: *Thermoelectric, Colloidal nanocrystals, Ligands, Metallic chalcogenides*

Colloidal synthesis shows great potential in many applications, including optoelectronics, biolabeling, catalysis, and thermoelectrics (TEs).[1−6] The synthesized colloidal nanocrystals usually consist of inorganic crystalline cores with layers of organic molecule ligands (e.g., oleic acid, trioctylphosphine oxide, alkanethiols, etc.) attached to their surfaces. The choice of ligands is of utmost importance for the colloidal stability NCs and the function of NC-based devices. The size, chemical composition, structure, and morphology of the nanocrystal cores are regulated by ligands during the nucleation and growth process, determining the physiochemical properties.[7,8] The interparticle distance, colloidal dispersion, and packing density of an NCs assembly determined by the ligand nature/coverage strongly affect the charge carrier transport property, thermal conductivity, and chemical reactivity.[9−13] For example, Wang et al. proposed a novel ligand-cross-linking process to increase the thermal conductivity of NC solids by overcoming the thermal-transport bottleneck between adjacent colloidal NCs.[14] Zheng et al. demonstrated that the unique ligand system could modify the active sites and improve the catalytic capability of PdAu bimetallic nanocluster catalysts.[15]

For TE materials, the performance is evaluated by the dimensionless figure of merit zT ($zT = S^2\sigma T/\kappa$, where S, σ, T, and κ are the Seebeck coefficient, electrical conductivity, absolute temperature, and thermal conductivity, respectively).[10,16,17] A good TE material requires a high power factor ($PF = S^2\sigma$) and low κ. An effective strategy to achieve depressed κ is to sinter ligand-assisted wet-chemistry-synthesized nanoparticles into dense nanostructured blocks, which enhance phonon scattering at numerous grain boundaries.[18] During assembly into semiconducting solids, the surface ligands are readily lost by thermally decomposing the organic ligands, chemically removing them, or replacing long organic ligands with shorter organic or inorganic ligands before sintering.[19−21] For instance, Yu et al.[22] removed organic ligands of large-scale colloidal $Cu_2ZnSnSe_4$ NCs by dealing with hydrazine before NCs consolidation. With this strategy, various materials such as Cu_2SnSe_3,[23] Bi_2Te_3,[24] $Cu_2CdSnSe_4$,[25] and Cu_5FeS_4[26] were sintered into pellets by spark plasma for TE applications. Maria Ibáñez et al.[27] removed ligands by heating the nanoparticle powders under inert gas before the hot press procedure. Talapin et al. investigated surface ligand exchange by metallic cation, halide anions, metal chalcogenide, and halide perovskites for NCs-ligand interface modification and optimized TE performance.[3,28−30] In addition, ligand

Received: April 17, 2023
Revised: May 18, 2023
Published: May 22, 2023

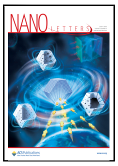

https://doi.org/10.1021/acs.nanolett.3c01438
Nano Lett. 2023, 23, 5317−5325

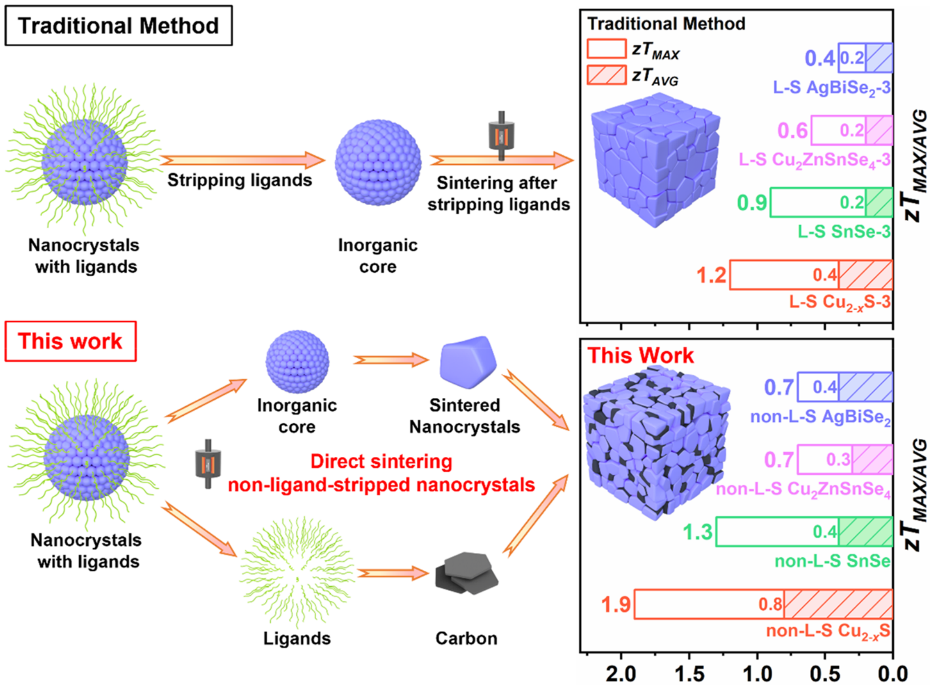

Figure 1. Schematic diagram of improving TE performance of the nanocrystals (SnSe, $Cu_{2-x}S$, $AgBiSe_2$, and $Cu_2ZnSnSe_4$) through retaining organic ligands.

exchange in commercial quantum dot light-emitting diodes frequently enhance charges transfer between quantum dots to improve quantum efficiency.[31−36] However, all these post-ligand treatments are multistep processes, which are cumbersome and costly.[4,9,37] Also, they often need expensive hydrazine or thiols, which are toxic or flammable. On the contrary, without stripping the organic ligands, the structure of the ligands can influence the assembled semiconductor nanocrystals and achieve their interfacial modification at the surfaces of NCs, which has rarely been studied and remains a challenge. This motivated us to delve into how ligand retaining can regulate the TE properties of colloidal NCs.

Herein, a new strategy to retain the ligands of TE nanomaterials is demonstrated in SnSe, $Cu_{2-x}S$, $AgBiSe_2$, and $Cu_2ZnSnSe_4$ NCs, in contrast to the traditional methods that strip the ligands. Ligand coatings can be partially retained and used as controllable molecular solders, simultaneously acting as precursors for forming secondary carbon phases during NCs consolidation. Calculations indicate that the introduced high-density organic−inorganic semiconductor interface suppresses the κ of the materials. As a result, compared with control samples (with ligand stripping), the samples without ligand stripping show higher peak and average zT values. In addition to excellent TE performance, $Cu_{2-x}S$ without ligand stripping shows improved mechanical properties, which provide the potential for device applications. The preparation method without ligand stripping reduces solvents and toxic reagents, enabling the cost-effective fabrication of efficient TE materials, a practical example of atom economy and green chemistry.

Figure 1 shows the synthesis processes, comparing the ligand-stripping and ligand-retaining methods. First, the nanoparticles are synthesized by a colloidal synthesis approach, which forms a layer of ligand molecules on the nanoparticle surfaces. Hydrazine, as a Brönsted base, traditionally removes the original capping ligands from the nanocrystal surfaces. Whether these nanoparticles are treated with hydrazine to remove ligand molecules or not, the process is named the ligand-stripping or ligand-retaining process. The nanoparticles are sintered into dense nanostructured blocks using Spark Plasma Sintering (SPS). As a proof of concept, we select SnSe (the record-high zT TE material), phonon-liquid electron-crystal $Cu_{2-x}S$, diamond-like structured $AgBiSe_2$, and multinary $Cu_2ZnSnSe_4$ with the commonly used long-alkyl-chain organic ligands (oleylamine (OAm), oleic acid (OA), and dodecanethiol (DDT)) as examples. The sintering and molding of as-synthesized nanocrystals lasted for 30 min in a closed die during SPS, preventing the volatilization of ligands. Therefore, the remaining organic ligands thermally decompose and transform into organic carbon as a secondary phase within the matrices, forming the inorganic NCs-organic carbon interface (Figures 1 and S1). Reduced κ in the non-L-S samples is attributed to residual carbon at the grain boundaries and the slightly smaller crystal domains than in the L-S samples. The well-developed surface chemistry of colloidal NCs by retained ligands offers the opportunity to engineer the interfaces and microstructures of the assembled solids, resulting in a high average zT and excellent mechanical properties. In this study, NCs treated with hydrazine hydrate for 0, 1, and 3 time(s) are referred to as non-L-S sample, L-S sample-1, and L-S sample-3, respectively.

The atomic structures of the samples are characterized through several techniques. The representative X-ray diffraction (XRD) patterns (Figure S2) demonstrate the crystalline structure of the SnSe, $Cu_{2-x}S$, $AgBiSe_2$, and $Cu_2ZnSnSe_4$ NCs, which are indexed to the orthorhombic $Pnma$ phase, tetragonal $P4_32_12$ and monoclinic $P2_1/c$ phase, hexagonal $P\bar{3}m1$ phase, and cubic $F\bar{4}3m$ phase, respectively. The hydrazine treatment does not change the crystal structure of the materials. Table S4 in the Supporting Information shows the cell parameters of the above materials. The transmission electron microscopy (TEM) images of the SnSe, $Cu_{2-x}S$, $AgBiSe_2$, and $Cu_2ZnSnSe_4$ NCs characterize the size distribution and morphology of as-

https://doi.org/10.1021/acs.nanolett.3c01438
Nano Lett. 2023, 23, 5317−5325

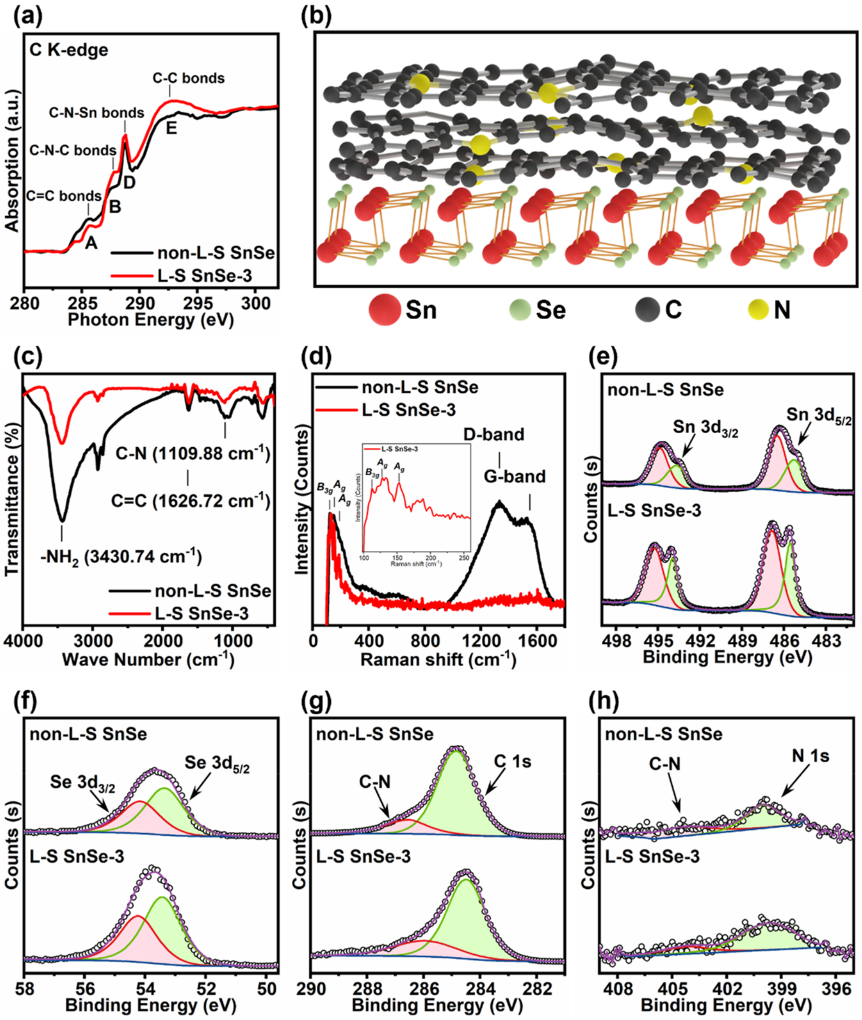

Figure 2. (a) C K-edge soft X-ray absorption near-edge spectroscopy (XANES) normalized spectra. (b) Schematic diagram of NCs surface morphology structure. (c) Fourier transform infrared (FTIR) and (d) Raman spectra of non-L-S SnSe and L-S SnSe-3. The XPS peak areas of (e) Sn 3d$_{3/2}$ and Sn 3d$_{5/2}$, (f) Se 3d$_{3/2}$ and Se 3d$_{5/2}$, (g) C 1s, and (h) N 1s of the non-L-S SnSe and L-S SnSe-3.

synthesized NCs (Figures 3a and S4). Disk-like, small sphere-like, irregular, and cubic shapes with average sizes of around 336 (±65) nm, 18 (±3) nm, 19 (±4) nm, and 13 (±2) nm are obtained for these four materials, respectively. The high-resolution (HR) TEM of SnSe, $Cu_{2-x}S$, $AgBiSe_2$, and $Cu_2ZnSnSe_4$ are shown in Figures 3b and S4.

To identify the chemical environment of the organic surfactant shell surrounding the TE materials before and after ligand stripping, we perform Fourier transform infrared (FTIR) spectroscopy for dried samples. As shown in Figure 2c, the presence of the OAm molecules is identified by the symmetric and asymmetric stretching vibrations of $-NH_2$ at 3430.74 cm^{-1}, the bending vibrations of C=C bonds at 1626.72 cm^{-1}, and the bending vibration of the C−N bond at 1109.88 cm^{-1}. These features are weaker in the L-S SnSe-3 sample compared with the nonstripped samples. The L-S SnSe-3 sample also shows the removal of ligands from the surface of colloidal nanoparticles by exchange with hydrazine. This result is in good accordance with Raman spectra (Figures 2d and S3), in which the carbon peaks of the samples are calibrated relative to the characteristic B_{3g} and A_g Raman modes of SnSe at 109, 128.5, and 150 cm^{-1}.[38,39] Two dominant carbon peaks of SPSed SnSe samples without ligand stripping at around 1334 and 1526 cm^{-1} correspond to the D and G bands, respectively (Figure 2d). The D band is assigned to the breathing mode of A_{1g} symmetry or sp^3-rich phase for the disordered graphite. The G band corresponds to the E_{2g} mode of 2D graphite, which is related to the vibration of sp^2-hybridized carbon. The D and G bands indicate that the surface ligands are turned into organic carbons during sintering. The relatively high intensity of the D-band and G-band (I_D/I_G) (1.11) for non-L-S SnSe indicates a high degree of carbon disorder, which is beneficial for enhancing phonon scattering and reducing thermal conductivity.[40−42] For SPSed L-S SnSe-3, the intensity of the D and G bands are significantly decreased due to the ligand stripping and the elimination of carbon during the annealing process.[41,42] This is also proved by carbon composition analysis. The carbon content (1.23 wt %) for SPSed non-L-S SnSe pellets was much higher than that (0.264 wt %) of L-S SnSe-3 pellets. In addition, the N atom in oleylamine ligands will incorporate into the nanostructure solids during the bulk consolidation step to provide a large density of point defects, facilitating the reduction of thermal conductivities (Figure 2b). To test the formation of the carbon-heteroatom bond, soft X-ray absorption near-edge structure (XANES) measurements are used to detect the K-edge excitation of elemental C (Figure 2a) to investigate the electronic structure and the nature of the carbon defect of the

SnSe-Carbon sample. Four peaks at ~285.5, 287.8, 288.7, and 292.1 eV are denoted as A, B, D, and E, respectively. The absorption peak A corresponds to π^* excitations of C═C bonds at the defect sites,[43] and the peak E corresponds to the σ^* structure of C−C bonds.[44] The strong π^* and σ^* bands structures show that the carbon is graphitized.[45] The weak shoulder peaks B and D exist between π^* and σ^* features, ascribed to the π^* excitation of C−N−C bonds in the g-C_3N_4 structure and C−N−Sn bridging bonds, respectively, demonstrating a stronger interfacial interaction between N-doped carbon and SnSe nanoparticles and the defective characteristics of the carbon layer.[43−45]

X-ray photoelectron spectroscopy (XPS) analysis further proves this phenomenon (Figure 2e−h). The Sn peaks of non-L-S SnSe are slightly shifted to lower binding energies (BEs) compared to the reported SnSe (~0.33 eV),[46] demonstrating the bonding of C−N−Sn. The same phenomenon has also occurred in the Se 3d spectra, shifting about 0.12 eV to lower BE. The fitting result of the N 1s peak shows that two peaks at 400.5 and 404.2 eV correspond to pyridinic-N and graphitic-N, and pyridinic-N is the dominant species.[44,45,47] The C 1s spectrum can be divided into two peaks at 284.8 eV and a higher BE of 286.6 eV, corresponding to the sp^2 hybridized graphitic carbon and C−N species.[48]

TEM images (Figure 3c,d) demonstrate that the $Cu_{2-x}S$ NCs are embedded in the nanostructured solids, and the ligands are carbonized as a carbon coating on the grain of $Cu_{2-x}S$. Figure 3d shows the d-spacing of carbon is approximately 0.41 nm.[49] The carbon is mainly distributed along with the marginal area of Cu and S elements, as depicted in the EDS elemental mapping in Figure 3g−j. The carbon coating of $Cu_{2-x}S$ is rarely observed in the ligand-stripped samples (Figure 3e), consistent with the FTIR, Raman, and carbon-content analysis results as discussed above. In addition, elemental mappings are performed to identify Sn, Se, Ag, Bi, Cu, and Zn elements in nanoparticles for SPSed SnSe, SPSed $AgBiSe_2$, and SPSed $Cu_2ZnSnSe_4$ (Figures S6−S8).

The TE properties of $Cu_{2-x}S$ are measured in the temperature range from 300 to 937 K (Figure 4). The dependence of the σ and the S on the temperature of non-L-S samples is similar to that of L-S samples. The electrical conductivity shows two peaks because of the phase transition, which is similar to the reports in the literature.[50,57] For non-L-S $Cu_{2-x}S$, the two peaks are 21.5×10^3 and 32.2×10^3 S m^{-1}at 323 and 650 K, respectively. Relatively high electrical conductivities were obtained for the ligand-stripped samples, and the carbon capping layer slightly affects the electric transport of the nonligand-stripped sample. The value of the S obtained for the $Cu_{2-x}S$ samples increases with temperature and decreases with increasing ligand stripping throughout the entire temperature. For example, as shown in Figure 4d, the room-temperature S for the non-L-S $Cu_{2-x}S$, L-S $Cu_{2-x}S$-1, and L-S $Cu_{2-x}S$-3 samples are 79.1, 74.5, and 58.3 μV·K^{-1}, respectively. Such difference is largely related to the n_H (Figure 4b), derived from the copper vacancy and the residual carbon at the grain boundaries. The non-L-S $Cu_{2-x}S$ with more carbon components have lower n_H, and alkaline hydrazine hydrate treatment can lead to the etching of the surface of NCs, in which the generation of metal vacancies will increase their n_H. Finally, the PF of all the samples is shown in Figure 4e. At 937 K, the PF of non-L-S $Cu_{2-x}S$ (0.97 mW m^{-1} K^{-2}) is higher than that of the L-S samples (0.90 mW m^{-1} K^{-2}) due to its higher S.

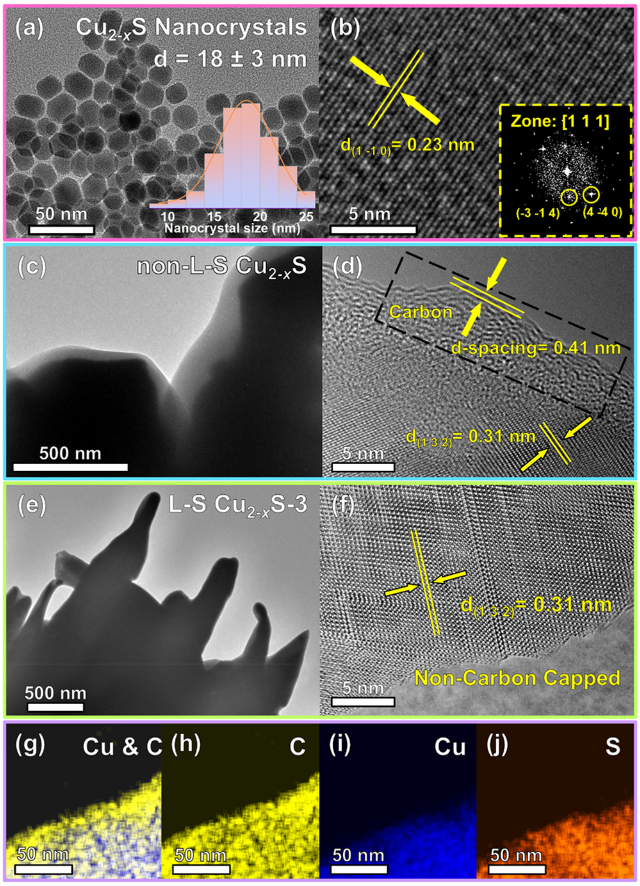

Figure 3. Morphology characterizations of $Cu_{2-x}S$ samples. (a) The TEM images with the grain size distribution histograms of the as-synthesized sphere-like $Cu_{2-x}S$ nanoparticles. (b) The HRTEM image of $Cu_{2-x}S$ nanoparticles. (inset) The corresponding FFT pattern. (c, d) TEM and HRTEM images of the non-L-S $Cu_{2-x}S$ sample, the carbon is marked in the black dashed box. (e, f) TEM and HRTEM images of the L-S $Cu_{2-x}S$-3. (g−j) The energy-dispersive spectroscopy (EDS) elemental mapping of C (yellow), Cu (blue), and S (orange) for non-L-S $Cu_{2-x}S$ sample.

The κ_{tot} (Figure 4g) of the non-L-S $Cu_{2-x}S$ pellet is 0.63 W m^{-1} K^{-1} at 323 K, which is lower than those of L-S $Cu_{2-x}S$-1 (0.73 W m^{-1} K^{-1}) and L-S $Cu_{2-x}S$-3 (0.83 W m^{-1} K^{-1}). According to the Wiedemann−Franz law, the electronic thermal conductivity can be calculated via $\kappa_{ele} = L\sigma T$, where $L = (1.5 + \exp(-|S|/116)) \times 10^{-8})$ is the Lorenz number. After subtracting κ_{ele} from κ_{tot}, we obtain the lattice thermal conductivity κ_{lat}, as shown in Figure 4f.[16,58] It is found that the κ_{lat} decreased by as much as 43% (from 0.35 to 0.20 W m^{-1} K^{-1}) upon retaining the ligands. Due to the slightly enhanced PF and much-reduced κ_{tot}, a high zT_{max} of 1.9 (at 937 K) is achieved for non-L-S $Cu_{2-x}S$ (Figure 4h). Figure 4i compares the zT values achieved in this work with the state-of-the-art peak zT in $Cu_{2-x}S$ compounds, indicating that the method of retaining ligands in this work positively impacts improving the TE properties. In addition, the theoretical maximum efficiency of 10% for the non-L-S $Cu_{2-x}S$ and a theoretical maximum figure of merit ZT of a TE device of the 0.5 for 320−930 K temperature range was calculated using the method provided by Snyder et al. (Figure S10).[59]

To understand the decreased lattice thermal conductivity with retaining ligands (or increasing amorphous carbon content), we conducted theoretical analyses using $Cu_{2-x}S$ as

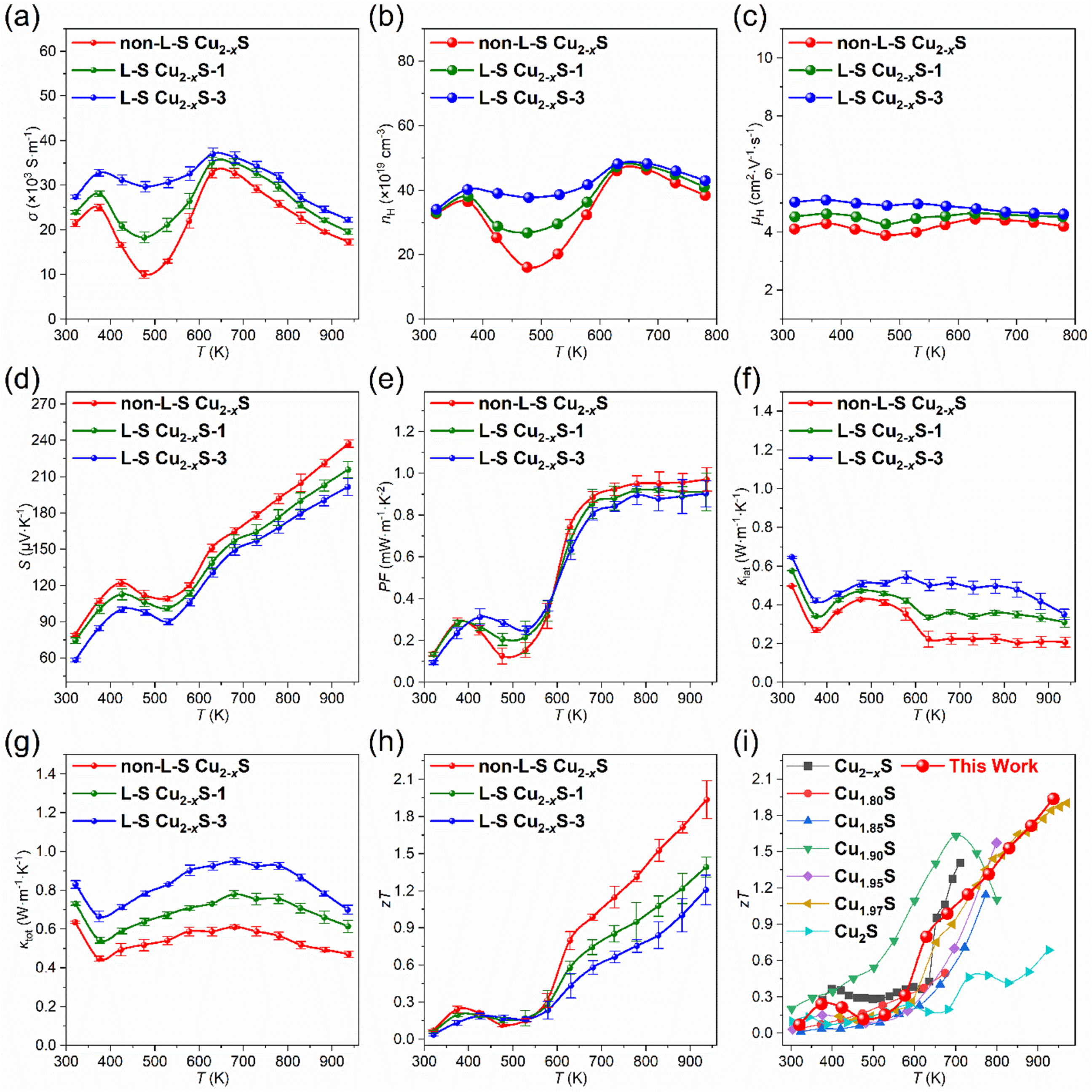

Figure 4. Temperature-dependent (a) electrical conductivity (σ), (b) carrier concentration (n_H), (c) carrier mobility (μ_H), (d) Seebeck coefficient (S), (e) power factor (PF), (f) lattice thermal conductivity (κ_{lat}), (g) total thermal conductivity (κ_{tot}), and (h) zT. (i) zTs of $Cu_{2-x}S$ TE materials.[50−56] Reprinted with permission from ref 50. Copyright [2021] [Wiley]. Reprinted with permission from ref 51. Copyright [2021] [ACS publications]. Reprinted with permission from ref 52. Copyright [2020] [Elsevier B.V.]. Reprinted with permission from ref 53. Copyright [2015] [RSC]. Reprinted with permission from ref 54. Copyright [2011] [RSC]. Reprinted with permission from ref 55. Copyright [2021] [Elsevier B.V.]. Reprinted with permission from ref 56. Copyright [2016] [Wiley].

an example. To estimate the interfacial thermal resistance (R_K) between Cu_2S and amorphous carbon, we calculated the phonon density of states (DOS) of Cu_2S by density functional theory (DFT). We collected the phonon DOS of different forms of carbon,[60,61] as shown in Figure 5b. It is found that they exhibit a great mismatch: Cu_2S has extremely high DOS below 10 THz, where the DOS of carbon is minimal, indicating that R_K should be very large. To estimate whether R_K can play a role in reducing the thermal conductivity of Cu_2S, we estimated R_K using the diffusive mismatch model (DMM)[62] (See page 7 of Supporting Information for detailed calculations).

Owing to the reduced κ and the increased PF, higher zT values of non-L-S $Cu_{2-x}S$ are achieved as 1.9 at 937 K, 1.6-fold of the value obtained by L-S $Cu_{2-x}S$-3 (zT = 1.2), indicating our strategy of retaining ligands affects improving TE performance (Figure 4f). To validate the potential of the described procedure to prepare nanomaterials with enhanced performance, in addition to $Cu_{2-x}S$, we obtained the TE properties of SnSe, $AgBiSe_2$, and $Cu_2ZnSnSe_4$ pellets (Figures S11−S13). Lower κ of non-L-S samples indicate the scattering

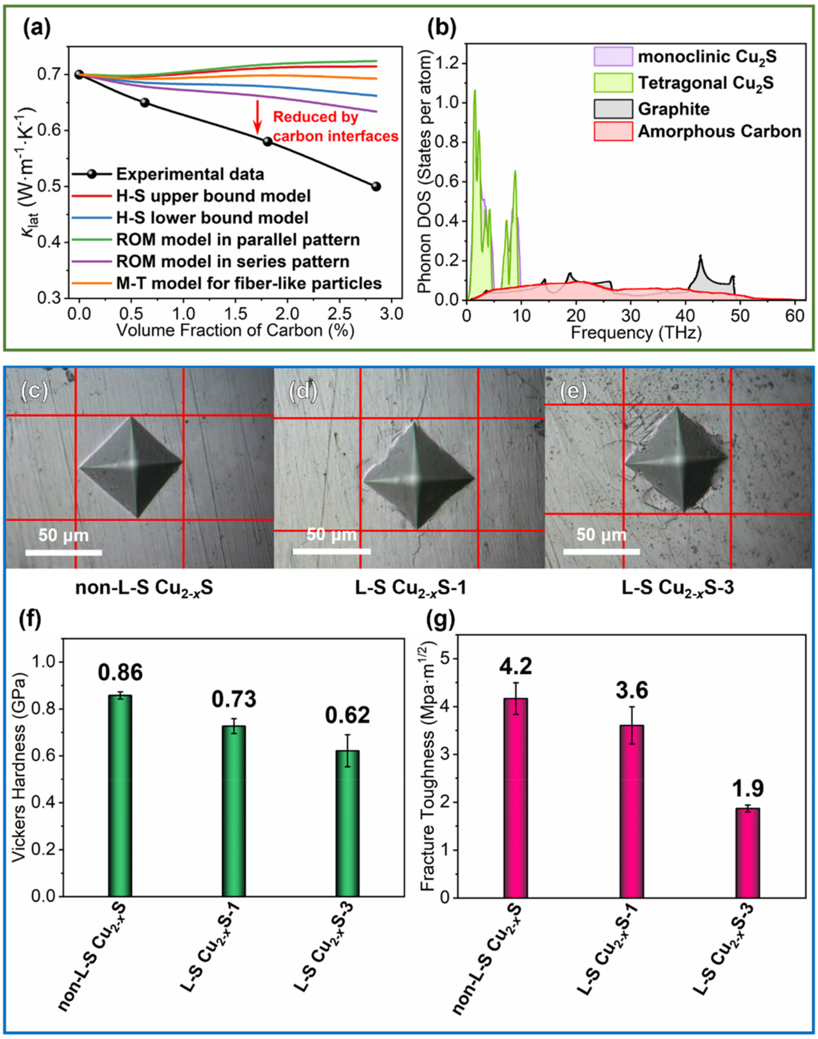

Figure 5. (a) Lattice thermal conductivity (κ_{lat}) at 323 K with different volume fractions of carbon. The thermal conductivities are predicted by the Hashin-Shtrikman bound model (H−S ub and H−S lb), the rule of mixture (ROM) model in parallel and series patterns, and the Mori-Tanaka (M-T) model for fiber-like particles. (b) The mismatch in phonon density of states between Cu_2S and different forms of carbon.[60,61] Reprinted with permission from ref 60. Copyright [2004] [Elsevier Ltd.]. Reprinted with permission from ref 61. Copyright [2018] [Informa UK Limited]. The microscopic appearance of indentation of the (c) non-L-S $Cu_{2-x}S$, (d) L-S $Cu_{2-x}S$-1, and (e) L-S $Cu_{2-x}S$-3. (f) Micro Vickers hardness and (g) fracture toughness of the non-L-S $Cu_{2-x}S$, L-S $Cu_{2-x}S$-1, and L-S $Cu_{2-x}S$-3.

of phonons at interfaces in these nanocrystalline alloy composites.

Finally, the zT values of the above non-L-S samples prepared by the retained ligands route are all higher than those of L-S sample-3 due to reduced κ_{tot} without deterioration of the electrical transport performance. As shown in Figure 1, the highest zT for the L-S SnSe-3, L-S $Cu_{2-x}S$-3, L-S $AgBiSe_2$-3, and L-S $Cu_2ZnSnSe_4$-3 are 0.9, 1.2, 0.4, and 0.6, respectively, while the highest zT for non-L-S samples are 1.3, 1.9, 0.7, and 0.7, respectively, and the average zT has a similar trend. We believe that the surface-ligand influence on properties is related to the effect of surface treatment on the final surface composition and structure. The inorganic NCs-organic carbon interfaces effectively scatter long mean-free-path electrons and phonons, which is beneficial to reducing the κ. Although the carbon-nano grain interfaces slightly, there is a decrease of the σ due to the insulating capping layer of carbon. Under certain conditions, they also play an important role in enhancing the S. Therefore, the zT can be improved by balancing the electronic and thermal properties by regulating the amount of retained organic ligands.

After we achieved an improved zT value, we also evaluated the fracture toughness to understand the effect of retained ligands on the mechanical properties (take the $Cu_{2-x}S$ system, for example). The Vickers hardness (H_v) and fracture toughness (K_{IC}) are measured on the polished surface according to the equations $H_v = 1854.4 \cdot F/D^2$ and $K_{IC} = A \cdot (E/H_v)^{0.5} \cdot (F/c^{1.5})$, where F is the applied load, D is the length of the diagonal of the resultant impression, the calibration constant is a value of 0.01,[63,64] c is the radial crack length of Vickers indentation, and E is Young's modulus of the $Cu_{2-x}S$ samples.[65] We use nanoindentation to measure Young's modulus. Figure 5f,g shows that the hardness and the fracture toughness of L-S $Cu_{2-x}S$-3 are about 0.62 GPa and 1.9 MPa·m$^{1/2}$, respectively. In contrast, the hardness and fracture toughness of the non-L-S $Cu_{2-x}S$ can reach as high as 0.86 GPa and 4.2 MPa·m$^{1/2}$. Ligands used as controllable molecular solders can generate a bridging effect between $Cu_{2-x}S$ grains and improve their stronger interaction, resulting in optimized mechanical durability.

In conclusion, we develop a general synthesis method to avoid complex ligand stripping procedures and introduce controlled amounts of secondary carbon phases. We have demonstrated that residual carbon between grain boundaries suppresses thermal conductivity and enhances the mechanical properties of NC solids. Furthermore, the convenience and potential of the strategy are demonstrated with SnSe, $Cu_{2-x}S$, $AgBiSe_2$, and $Cu_2ZnSnSe_4$ NCs, which possess higher *zTs* as compared to control samples with ligand stripping. Our result provides a general route for suppressing thermal transport in organic/inorganic hybrid materials. Beyond the above metallic chalcogenides in this work, the strategy will likely be broadly applicable to other colloidal nanomaterials. It should help to expand interface engineering to other device applications, such as photovoltaics, electronics, and light-emitting diodes.

■ ASSOCIATED CONTENT

Supporting Information

The Supporting Information is available free of charge at https://pubs.acs.org/doi/10.1021/acs.nanolett.3c01438.

> Details of the experimental section, density functional theory calculation (Tables S1−S3), additional X-ray diffraction patterns (Figure S2), additional transmission electron microscopy, and scanning electron microscopy analyses (Figures S4−S9 and S14), and TE properties of SnSe, $AgBiSe_2$, and $Cu_2ZnSnSe_4$ (Figures S10−S13) (PDF)

■ AUTHOR INFORMATION

Corresponding Author

Biao Xu − *School of Chemistry and Chemical Engineering, Nanjing University of Science and Technology, Nanjing 210094, China; Chemical Engineering, Collaborative Innovation Center of Advanced Microstructures, Nanjing University, Nanjing 210093, China;* orcid.org/0000-0002-6645-3905; Email: xubiao@njust.edu.cn

Authors

Yue Lou − *School of Chemistry and Chemical Engineering, Nanjing University of Science and Technology, Nanjing 210094, China;* orcid.org/0000-0002-0364-6582

Xiaokun Li − *School of Chemistry and Chemical Engineering, Nanjing University of Science and Technology, Nanjing 210094, China;* orcid.org/0000-0002-0342-594X

Zhan Shi − *State Key Laboratory of Inorganic Synthesis and Preparative Chemistry, College of Chemistry, Jilin University, Changchun 130012, China;* orcid.org/0000-0001-9717-1487

Hao Zhou − *Department of Mechanical Engineering, The University of Utah, Salt Lake City 84112 Utah, USA;* orcid.org/0000-0001-6499-1921

Tianli Feng − *Department of Mechanical Engineering, The University of Utah, Salt Lake City 84112 Utah, USA;* orcid.org/0000-0002-7284-5657

Complete contact information is available at: https://pubs.acs.org/10.1021/acs.nanolett.3c01438

Author Contributions

$^{\perp}$Y.L. and X.K.L. contributed equally.

Notes

The authors declare no competing financial interest.

■ ACKNOWLEDGMENTS

B.X. is thankful for the financial support from "the Fundamental Research Funds for the Central Universities," No. 30922010201, and the Key Laboratory for Soft Chemistry and Functional Materials of the Ministry of Education, Nanjing University of Science and Technology. Y.L. is thankful for financial support from the Jiangsu Provincial Innovation and Entrepreneurship Doctor Program (JSSCBS20210215). H.Z. and T.F. thank the National Science Foundation (NSF Award No. 2212830) for the support. The calculation used the NSF Extreme Science and Engineering Discovery Environment (XSEDE). This research also used resources of the National Energy Research Scientific Computing Center, a Department of Energy (DOE) Office of Science User Facility supported by the Office of Science of the U.S. DOE under Contract No. DE-AC02-05CH11231 using NERSC Award No. BES-ERCAP0022132. The support and resources from the Center for High-Performance Computing at the University of Utah are gratefully acknowledged.

■ REFERENCES

(1) Coughlan, C.; Ibanez, M.; Dobrozhan, O.; Singh, A.; Cabot, A.; Ryan, K. M. Compound Copper Chalcogenide Nanocrystals. *Chem. Rev.* **2017**, *117* (9), 5865−6109.

(2) Kovalenko, M. V.; Manna, L.; Cabot, A.; Hens, Z.; Talapin, D. V.; Kagan, C. R.; Klimov, V. I.; Rogach, A. L.; Reiss, P.; Milliron, D. J.; et al. Prospects of Nanoscience with Nanocrystals. *ACS Nano* **2015**, *9* (2), 1012−1057.

(3) Kovalenko, M. V.; Scheele, M.; Talapin, D. V. Colloidal Nanocrystals with Molecular Metal Chalcogenide Surface Ligands. *Science* **2009**, *324* (5933), 1417.

(4) Ortega, S.; Ibáñez, M.; Liu, Y.; Zhang, Y.; Kovalenko, M. V.; Cadavid, D.; Cabot, A. Bottom-up engineering of thermoelectric nanomaterials and devices from solution-processed nanoparticle building blocks. *Chem. Soc. Rev.* **2017**, *46* (12), 3510−3528.

(5) Zhao, L.-D.; Qin, B.; Liu, D. SnSe/SnS: Multifunctions Beyond Thermoelectricity. *Mater. Lab* **2022**, *1* (1), 1.

(6) Xiao, Y. Routes to High-Ranged Thermoelectric Performance. *Mater. Lab* **2022**, *1* (3), 1 DOI: 10.54227/mlab.20220025.

(7) Dong, X.; Cui, M.; Huang, R.; Su, R.; Qi, W.; He, Z. Polydopamine-Assisted Surface Coating of MIL-53 and Dodecanethiol on a Melamine Sponge for Oil-Water Separation. *Langmuir* **2020**, *36* (5), 1212−1220.

(8) Fan, F.-J.; Wu, L.; Yu, S.-H. Energetic I−III−VI2and I2−II−IV−VI4nanocrystals: synthesis, photovoltaic and thermoelectric applications. *Energy Environ. Sci.* **2014**, *7* (1), 190−208.

(9) Heuer-Jungemann, A.; Feliu, N.; Bakaimi, I.; Hamaly, M.; Alkilany, A.; Chakraborty, I.; Masood, A.; Casula, M. F.; Kostopoulou, A.; Oh, E.; et al. The Role of Ligands in the Chemical Synthesis and Applications of Inorganic Nanoparticles. *Chem. Rev.* **2019**, *119* (8), 4819−4880.

(10) Wu, Z.; Zhang, S.; Liu, Z.; Mu, E.; Hu, Z. Thermoelectric converter: Strategies from materials to device application. *Nano Energy* **2022**, *91*, 106692.

(11) Zhang, Q.; Deng, K.; Wilkens, L.; Reith, H.; Nielsch, K. Micro-thermoelectric devices. *Nat. Electron.* **2022**, *5* (6), 333−347.

(12) Wang, Z.; Schliehe, C.; Bian, K.; Dale, D.; Bassett, W. A.; Hanrath, T.; Klinke, C.; Weller, H. Correlating Superlattice Polymorphs to Internanoparticle Distance, Packing Density, and Surface Lattice in Assemblies of PbS Nanoparticles. *Nano Lett.* **2013**, *13* (3), 1303−1311.

(13) Zhao, L.; Qin, B. Carriers: the Less, the Faster. *Mater. Lab* **2022**, *1* (1), 1.

(14) Wang, Z.; Singaravelu, A. S. S.; Dai, R.; Nian, Q.; Chawla, N.; Wang, R. Y. Ligand Crosslinking Boosts Thermal Transport in Colloidal Nanocrystal Solids. *Angew. Chem., Int. Ed.* **2020**, *59* (24), 9556−9563.

(15) Shen, H.; Wu, Q.; Asre Hazer, M. S.; Tang, X.; Han, Y.-Z.; Qin, R.; Ma, C.; Malola, S.; Teo, B. K.; Hakkinen, H.; Zheng, N.; et al. Regioselective hydrogenation of alkenes over atomically dispersed Pd sites on NHC-stabilized bimetallic nanoclusters. *Chem.* **2022**, *8* (9), 2380−2392.

(16) Tan, G.; Zhao, L. D.; Kanatzidis, M. G. Rationally Designing High-Performance Bulk Thermoelectric Materials. *Chem. Rev.* **2016**, *116* (19), 12123−12149.

(17) Finefrock, S. W.; Yang, H.; Fang, H.; Wu, Y. Thermoelectric Properties of Solution Synthesized Nanostructured Materials. *Annu. Rev. Chem. Biomol. Eng.* **2015**, *6* (1), 247−266.

(18) He, J.; Wu, D.; Zhang, F. The Roles of Grain Boundaries in Thermoelectric Transports. *Mater. Lab* **2022**, *1* (1), 1 DOI: 10.54227/mlab.20220012.

(19) Park, K.; Son, J. S.; Woo, S. I.; Shin, K.; Oh, M.-W.; Park, S.-D.; Hyeon, T. Colloidal synthesis and thermoelectric properties of La-doped $SrTiO_3$ nanoparticles. *J. Mater. Chem. A* **2014**, *2* (12), 4217−4224.

(20) Ibáñez, M.; Cadavid, D.; Zamani, R.; García-Castelló, N.; Izquierdo-Roca, V.; Li, W.; Fairbrother, A.; Prades, J. D.; Shavel, A.; Arbiol, J.; et al. Composition Control and Thermoelectric Properties of Quaternary Chalcogenide Nanocrystals: The Case of Stannite $Cu_2CdSnSe_4$. *Chem. Mater.* **2012**, *24* (3), 562−570.

(21) Ibanez, M.; Luo, Z.; Genc, A.; Piveteau, L.; Ortega, S.; Cadavid, D.; Dobrozhan, O.; Liu, Y.; Nachtegaal, M.; Zebarjadi, M.; et al. High-performance thermoelectric nanocomposites from nanocrystal building blocks. *Nat. Commun.* **2016**, *7* (1), 10766.

(22) Fan, F. J.; Wang, Y. X.; Liu, X. J.; Wu, L.; Yu, S. H. Large-scale colloidal synthesis of non-stoichiometric $Cu_2ZnSnSe_4$ nanocrystals for thermoelectric applications. *Adv. Mater.* **2012**, *24* (46), 6158−6163.

(23) Song, J. M.; Liu, Y.; Niu, H. L.; Mao, C. J.; Cheng, L. J.; Zhang, S. Y.; Shen, Y. H. Hot-injection synthesis and characterization of monodispersed ternary Cu_2SnSe_3 nanocrystals for thermoelectric applications. *J. Alloys Compd. and Compounds* **2013**, *581*, 646−652.

(24) Scheele, M.; Oeschler, N.; Meier, K.; Kornowski, A.; Klinke, C.; Weller, H. Synthesis and Thermoelectric Characterization of Bi_2Te_3 Nanoparticles. *Adv. Funct. Mater.* **2009**, *19* (21), 3476−3483.

(25) Fan, F. J.; Yu, B.; Wang, Y. X.; Zhu, Y. L.; Liu, X. J.; Yu, S. H.; Ren, Z. Colloidal synthesis of $Cu_2CdSnSe_4$ nanocrystals and hot-pressing to enhance the thermoelectric figure-of-merit. *J. Am. Chem. Soc.* **2011**, *133* (40), 15910−15913.

(26) Zhang, A.; Zhang, B.; Lu, W.; Xie, D.; Ou, H.; Han, X.; Dai, J.; Lu, X.; Han, G.; Wang, G.; et al. Twin Engineering in Solution-Synthesized Nonstoichiometric Cu_5FeS_4 Icosahedral Nanoparticles for Enhanced Thermoelectric Performance. *Adv. Funct. Mater.* **2018**, *28* (10), 1705117.

(27) Ibáñez, M.; Zamani, R.; Li, W.; Cadavid, D.; Gorsse, S.; Katcho, N. A.; Shavel, A.; López, A. M.; Morante, J. R.; Arbiol, J.; et al. Crystallographic Control at the Nanoscale To Enhance Functionality: Polytypic Cu_2GeSe_3 Nanoparticles as Thermoelectric Materials. *Chem. Mater.* **2012**, *24* (23), 4615−4622.

(28) Cadavid, D.; Ibáñez, M.; Shavel, A.; Durá, O. J.; López De La Torre, M. A.; Cabot, A. Organic ligand displacement by metal salts to enhance nanoparticle functionality: thermoelectric properties of Ag_2Te. *J. Mater. Chem. A* **2013**, *1* (15), 4864.

(29) Ibáñez, M.; Korkosz, R. J.; Luo, Z.; Riba, P.; Cadavid, D.; Ortega, S.; Cabot, A.; Kanatzidis, M. G. Electron Doping in Bottom-Up Engineered Thermoelectric Nanomaterials through HCl-Mediated Ligand Displacement. *J. Am. Chem. Soc.* **2015**, *137* (12), 4046−4049.

(30) Ibáñez, M.; Hasler, R.; Genç, A.; Liu, Y.; Kuster, B.; Schuster, M.; Dobrozhan, O.; Cadavid, D.; Arbiol, J.; Cabot, A.; et al. Ligand-Mediated Band Engineering in Bottom-Up Assembled SnTe Nanocomposites for Thermoelectric Energy Conversion. *J. Am. Chem. Soc.* **2019**, *141* (20), 8025−8029.

(31) Nguyen, H. T.; Duong, A. T.; Lee, S. Investigation the effect of different surface ligand treatments on luminescence and performance of quantum dot LEDs. *J. Mater. Res.* **2021**, *36* (16), 3309−3316.

(32) Qiu, Y. L.; Gong, Z. P.; Xu, L.; Huang, Q. C.; Yang, Z. X.; Ye, B. Q.; Ye, Y. L.; Meng, Z. Y.; Zeng, Z. W.; Shen, Z. H.; et al. Performance Enhancement of Quantum Dot Light-Emitting Diodes via Surface Modification of the Emitting Layer. *ACS Appl. Nano Mater.* **2022**, *5* (2), 2962−2972.

(33) Chen, J.; Shen, Z.; Liu, P.; Sun, Z.; Liu, J. G.; Shen, C.; Song, D.; Zhao, S.; Xu, Z. Synergistic function of doping and ligand engineering to enhance the photostability and electroluminescence performance of $CsPbBr_3$ quantum dots. *Nanotechnology* **2021**, *32* (32), 325202.

(34) Chen, W. W.; Tang, X. S.; Wangyang, P. H.; Yao, Z. Q.; Zhou, D.; Chen, F. G.; Li, S. Q.; Lin, H.; Zeng, F. J.; Wu, D. F.; et al. Surface-Passivated Cesium Lead Halide Perovskite Quantum Dots: Toward Efficient Light-Emitting Diodes with an Inverted Sandwich Structure. *Adv. Opt Mater.* **2018**, *6* (14), 1800007.

(35) Zhang, Q.; Jiang, M. H.; Yan, G. J.; Feng, Y. Q.; Zhang, B. Surface ligand engineering involving fluorophenethyl ammonium for stable and strong emission $CsPbBr_3$ quantum dots and high-performance QLEDs. *J. Mater. Chem. C* **2022**, *10* (15), 5849−5855.

(36) Zhao, B.; Chen, L.; Liu, W.; Wu, L.; Lu, Z.; Cao, W. High efficiency blue light-emitting devices based on quantum dots with core-shell structure design and surface modification. *RSC Adv.* **2021**, *11* (23), 14047−14052.

(37) Yazdani, S.; Pettes, M. T. Nanoscale self-assembly of thermoelectric materials: a review of chemistry-based approaches. *Nanotechnology* **2018**, *29* (43), 432001.

(38) Karthikeyan, V.; Oo, S. L.; Surjadi, J. U.; Li, X.; Theja, V. C. S.; Kannan, V.; Lau, S. C.; Lu, Y.; Lam, K.-H.; Roy, V. A. L. Defect Engineering Boosted Ultrahigh Thermoelectric Power Conversion Efficiency in Polycrystalline SnSe. *ACS Appl. Mater. Interfaces* **2021**, *13* (49), 58701−58711.

(39) Ludemann, M.; Gordan, O. D.; Zahn, D. R. T.; Beekman, M.; Atkins, R.; Johnson, D. C. Raman Spectroscopy Insights into the Size-Induced Structural Transformation in SnSe Nanolayers. *Langmuir* **2014**, *30* (27), 8209−8214.

(40) Yang, G.; Sang, L.; Yun, F. F.; Mitchell, D. R. G.; Casillas, G.; Ye, N.; See, K.; Pei, J.; Wang, X.; Li, J. F.; et al. Significant Enhancement of Thermoelectric Figure of Merit in BiSbTe-Based Composites by Incorporating Carbon Microfiber. *Adv. Funct. Mater.* **2021**, *31* (15), 2008851.

(41) Wang, K.; Zhao, N.; Lei, S.; Yan, R.; Tian, X.; Wang, J.; Song, Y.; Xu, D.; Guo, Q.; Liu, L. Promising biomass-based activated carbons derived from willow catkins for high performance supercapacitors. *Electrochim. Acta* **2015**, *166*, 1−11.

(42) Sevilla, M.; Fuertes, A. B. Direct Synthesis of Highly Porous Interconnected Carbon Nanosheets and Their Application as High-Performance Supercapacitors. *ACS Nano* **2014**, *8* (5), 5069−5078.

(43) Xu, H.; She, X.; Fei, T.; Song, Y.; Liu, D.; Li, H.; Yang, X.; Yang, J.; Li, H.; Song, L.; et al. Metal-Oxide-Mediated Subtractive Manufacturing of Two-Dimensional Carbon Nitride for High-Efficiency and High-Yield Photocatalytic H_2 Evolution. *ACS Nano* **2019**, *13* (10), 11294−11302.

(44) Wang, W.; Shang, L.; Chang, G.; Yan, C.; Shi, R.; Zhao, Y.; Waterhouse, G. I. N.; Yang, D.; Zhang, T. Intrinsic Carbon-Defect-Driven Electrocatalytic Reduction of Carbon Dioxide. *Adv. Mater.* **2019**, *31* (19), 1808276.

(45) Liu, D.; Wu, C.; Chen, S.; Ding, S.; Xie, Y.; Wang, C.; Wang, T.; Haleem, Y. A.; ur Rehman, Z.; Sang, Y.; et al. In situ trapped high-density single metal atoms within graphene: Iron-containing hybrids as representatives for efficient oxygen reduction. *Nano Res.* **2018**, *11* (4), 2217−2228.

(46) Saini, S.; Mele, P.; Tiwari, A. Influence of the planar orientation of the substrate on thermoelectric response of SnSe thin films. *J. Phys. Chem. Solids* **2019**, *129*, 347−353.

(47) Ye, X.; Lin, Z.; Liang, S.; Huang, X.; Qiu, X.; Qiu, Y.; Liu, X.; Xie, D.; Deng, H.; Xiong, X.; et al. Upcycling of Electroplating Sludge

into Ultrafine Sn@C Nanorods with Highly Stable Lithium Storage Performance. *Nano Lett.* **2019**, *19* (3), 1860−1866.

(48) Chang, X.; Wang, T.; Liu, Z.; Zheng, X.; Zheng, J.; Li, X. Ultrafine Sn nanocrystals in a hierarchically porous N-doped carbon for lithium ion batteries. *Nano Res.* **2017**, *10* (6), 1950−1958.

(49) Yoo, E.; Kim, J.; Hosono, E.; Zhou, H.-S.; Kudo, T.; Honma, I. Large Reversible Li Storage of Graphene Nanosheet Families for Use in Rechargeable Lithium Ion Batteries. *Nano Lett.* **2008**, *8* (8), 2277−2282.

(50) Yu, Y.; Yang, D.; Li, J.; Zhang, M.; Luo, H.; Liang, Q.; Ye, H.; Zhang, Q.; Tang, X.; Wu, J. A Flash Vacuum-Induced Reaction in Preparing High Performance Thermoelectric Cu_2S. *Adv. Funct. Mater.* **2022**, *32* (2), 2107284.

(51) Li, M.; Liu, Y.; Zhang, Y.; Han, X.; Zhang, T.; Zuo, Y.; Xie, C.; Xiao, K.; Arbiol, J.; Llorca, J.; et al. Effect of the Annealing Atmosphere on Crystal Phase and Thermoelectric Properties of Copper Sulfide. *ACS Nano* **2021**, *15* (3), 4967−4978.

(52) Nieroda, P.; Leszczynski, J.; Mikula, A.; Mars, K.; Kruszewski, M. J.; Kolezynski, A. Thermoelectric properties of Cu_2S obtained by high temperature synthesis and sintered by IHP method. *Ceram. Int.* **2020**, *46* (16), 25460−25466.

(53) Zhao, L.; Wang, X.; Fei, F. Y.; Wang, J.; Cheng, Z.; Dou, S.; Wang, J.; Snyder, G. J. High thermoelectric and mechanical performance in highly dense $Cu_{2-x}S$ bulks prepared by a melt-solidification technique. *J. Mater. Chem. A* **2015**, *3* (18), 9432−9437.

(54) Ge, Z. H.; Zhang, B. P.; Chen, Y. X.; Yu, Z. X.; Liu, Y.; Li, J. F. Synthesis and transport property of $Cu_{1.8}S$ as a promising thermoelectric compound. *Chem. Commun.* **2011**, *47* (47), 12697−12699.

(55) Nkemeni, D. S.; Yang, Z.; Lou, S. Y.; Li, G. H.; Zhou, S. M. Achievement of extra-high thermoelectric performance in doped copper (I) sulfide. *J. Alloys Compd.* **2021**, *878*, 160128.

(56) Ge, Z.-H.; Liu, X.; Feng, D.; Lin, J.; He, J. High-Performance Thermoelectricity in Nanostructured Earth-Abundant Copper Sulfides Bulk Materials. *Adv. Energy Mater.* **2016**, *6* (16), 1600607.

(57) He, Y.; Day, T.; Zhang, T.; Liu, H.; Shi, X.; Chen, L.; Snyder, G. J. High thermoelectric performance in non-toxic earth-abundant copper sulfide. *Adv. Mater.* **2014**, *26* (23), 3974−3978.

(58) Snyder, G. J.; Toberer, E. S. Complex thermoelectric materials. *Nat. Mater.* **2008**, *7* (2), 105−114.

(59) Snyder, G. J.; Snyder, A. H. Figure of merit ZT of a thermoelectric device defined from materials properties. *Energy Environ. Sci.* **2017**, *10* (11), 2280−2283.

(60) Wirtz, L.; Rubio, A. The phonon dispersion of graphite revisited. *Solid State Commun.* **2004**, *131* (3), 141−152.

(61) Sosso, G. C.; Deringer, V. L.; Elliott, S. R.; Csányi, G. Understanding the thermal properties of amorphous solids using machine-learning-based interatomic potentials. *Mol. Simul.* **2018**, *44* (11), 866−880.

(62) Kakodkar, R. R.; Feser, J. P. Probing the validity of the diffuse mismatch model for phonons using atomistic simulations. *Phys. Rev. B* **2017**, *95* (12), 125434.

(63) Anstis, G. R.; Chantikul, P.; Lawn, B. R.; Marshall, D. B. A Critical Evaluation of Indentation Techniques for Measuring Fracture Toughness: I, Direct Crack Measurements. *J. Am. Ceram. Soc.* **1981**, *64* (9), 533−538.

(64) Drory, M. D.; Ager, J. W.; Suski, T.; Grzegory, I.; Porowski, S. Hardness and fracture toughness of bulk single crystal gallium nitride. *Appl. Phys. Lett.* **1996**, *69* (26), 4044−4046.

(65) Jiang, B.; Liu, X.; Wang, Q.; Cui, J.; Jia, B.; Zhu, Y.; Feng, J.; Qiu, Y.; Gu, M.; Ge, Z.; et al. Realizing high-efficiency power generation in low-cost PbS-based thermoelectric materials. *Energy Environ. Sci.* **2020**, *13* (2), 579−591.

NANO LETTERS

pubs.acs.org/NanoLett Addition/Correction

Correction to “General Syntheses of High-Performance Thermoelectric Nanostructured Solids without Post-Synthetic Ligand Stripping”

Yue Lou, Xiaokun Li, Zhan Shi, Hao Zhou, Tianli Feng, and Biao Xu*

Nano Lett. **2023** *23* (11), 5317−5325. DOI: 10.1021/acs.nanolett.3c01438

Cite This: https://doi.org/10.1021/acs.nanolett.4c02556 Read Online

ACCESS | Metrics & More | Article Recommendations

The authors report a mistake in the acknowledgment section. The correct acknowledgment section should read as given below.

ACKNOWLEDGMENTS

B.X. is thankful for the financial support from “the Fundamental Research Funds for the Central Universities,” No. 30922010201, and the Key Laboratory for Soft Chemistry and Functional Materials of the Ministry of Education, Nanjing University of Science and Technology. Y.L. is thankful for financial support from the Jiangsu Provincial Innovation and Entrepreneurship Doctor Program (JSSCBS20210215). The support and resources from the Center for High-Performance Computing at the University of Utah are gratefully acknowledged.